DIII-D research towards establishing the scientific basis for future fusion reactors

C.C. Petty and the DIII-D Team

General Atomics, San Diego, CA, United States of America

E-mail: petty@fusion.gat.com

CrossMark

Abstract

DIII-D research is addressing critical challenges in preparation for ITER and the next generation of fusion devices through focusing on plasma physics fundamentals that underpin key fusion goals, understanding the interaction of disparate core and boundary plasma physics, and developing integrated scenarios for achieving high performance fusion regimes. Fundamental investigations into fusion energy science find that anomalous dissipation of runaway electrons (RE) that arise following a disruption is likely due to interactions with RE-driven kinetic instabilities, some of which have been directly observed, opening a new avenue for RE energy dissipation using naturally excited waves. Dimensionless parameter scaling of intrinsic rotation and gyrokinetic simulations give a predicted ITER rotation profile with significant turbulence stabilization. Coherence imaging spectroscopy confirms near sonic flow throughout the divertor towards the target, which may account for the convection-dominated parallel heat flux. Core-boundary integration studies show that the small angle slot divertor achieves detachment at lower density and extends plasma cooling across the divertor target plate, which is essential for controlling heat flux and erosion. The Super H-mode regime has been extended to high plasma current (2.0 MA) and density to achieve very high pedestal pressures (~30 kPa) and stored energy (3.2 MJ) with $H_{98y2} \approx 1.6$–2.4. In scenario work, the ITER baseline $Q = 10$ scenario with zero injected torque is found to have a fusion gain metric $\beta \tau_E$ independent of current between $q_{95} = 2.8$–3.7, and a lower limit of pedestal rotation for RMP ELM suppression has been found. In the wide pedestal QH-mode regime that exhibits improved performance and no ELMs, the start-up counter torque has been eliminated so that the entire discharge uses ≈ 0 injected torque and the operating space is more ITER-relevant. Finally, the high-β_N ($\leqslant 3.8$) hybrid scenario has been extended to the high-density levels necessary for radiating divertor operation, achieving ~40% divertor heat flux reduction using either argon or neon with P_{tot} up to 15 MW.

Keywords: fusion, plasma, tokamak, energy, DIII-D

(Some figures may appear in colour only in the online journal)

1. Introduction

The central theme of the DIII-D research program is to establish the scientific basis and operational knowledge for ITER and future fusion reactors using its unique capabilities. The role of DIII-D in the world's fusion energy program can be understood through three modi: the scientific investigation of plasma physics fundamentals, many of which are portable to other innovative toroidal concepts; understanding how disparate core and boundary plasma physics interact, an issue for all fusion devices in scaling to burning plasma conditions; and the development of attractive scenarios that address critical challenges in preparation for ITER [1] and the next generation of tokamak fusion devices. Scenario development is in many

respects the final product of fusion research, where self-consistent, integrated operational regimes for burning plasmas are pursued by a diverse team whose members pool their expertise in different topical science areas. Results contained in the paper have capitalized on several key hardware enhancements in the DIII-D facility, including the small angle slot (SAS) divertor, new power supplies to increase flexibility of applied 3D fields, new types of pellets and tungsten tile inserts, as well as new diagnostics enhancements such as surface-eroding thermocouples, coherence imaging spectroscopy (CIS), an imaging neutral particle analyzer and laser blow off (LBO). Recent results also exploit the existing machine flexibility, e.g. plasma shape control, variable perveance neutral beam injection (NBI), a wide range of NBI torque profiles using a mix of co- and counter-injected beams, adjustable current drive profiles especially from electron cyclotron current drive (ECCD), and variable ion/electron heating profiles.

The paper is organized as follows. Section 2 describes key fusion-enabling advances in disruption mitigation, energetic particle physics, turbulence and transport, and the physics of divertor detachment. Core-Edge integration is discussed in section 3, encompassing the newly-installed SAS divertor that gives detachment at lower core collisionality, the effect of divertor closure on pedestal structure, the impacts of resonant magnetic perturbations (RMP) on the plasma edge and L–H transition, and high pedestal pressures in Super H-mode. Advances in low-torque operation of both the ITER baseline scenario and the quiescent high confinement mode (QH-mode), the extension of the high-β_P regime to lower safety factor using reverse magnetic shear, and the integration of the high-β_N hybrid scenario with a radiative divertor are described in section 4. Finally, section 5 gives a summary of achievements and discusses planned upgrades and the future direction of the DIII-D program.

2. Advances in fusion energy science

Foundational science studies encourage in depth study of physical mechanisms that underpin key fusion goals. In this section, advances in fusion energy science from recent DIII-D experiments will be discussed in the disruption, energetic particle, turbulent transport and boundary physics areas.

2.1. Disruption physics

As full current disruptions in ITER may damage the first wall and vessel components if left unmitigated, DIII-D research places a high priority on establishing the principles and techniques for ITER's disruption mitigation system. Experiments on DIII-D have injected multiple shattered pellets at different toroidal locations for the first time [2], as is planned for the ITER disruption mitigation system. Systematically varying the relative timing of the two shattered pellets suggests that simultaneously injected pellets may impact the assimilation of each other, altering the resulting disruption characteristics. As seen in figure 1(a), thermal quench (TQ) radiation fractions measured near the injection location are reduced with the dual pellets (black diamonds) compared to the single pure
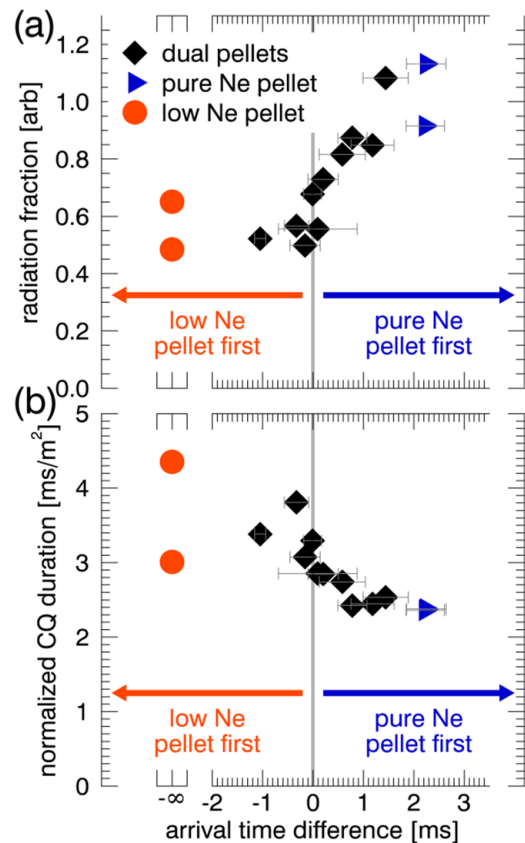

Figure 1. Dependence of (*a*) radiative power fraction and (*b*) normalized current quench duration on relative timing of pellets.

neon pellet (blue triangles) despite having similar injected neon quantities. Figure 1(*b*) shows that mitigation of current quench loads is also similarly reduced in the dual pellet cases, consistent with the observed reduction in TQ mitigation. These results suggest that extrapolating single pellet results to ITER may underestimate the required injection quantities for its multiple-pellet disruption mitigation system.

New energy-resolved measurements of hard x-ray (HXR) flux identify dissipation mechanisms for runaway electron (RE) populations that may arise after a disruption. Measurements with a unique gamma-ray imaging (GRI) system demonstrate that the observed anomalous dissipation in low density scenarios (cast in terms of the applied electric field E significantly exceeding the critical electric field E_{crit}) of RE beams is strongest for low energy RE populations [3, 4]. This can be largely understood by including the self-consistent interaction of the RE population with RE-driven kinetic instabilities that arise from strong wave-particle interactions with the low energy RE population (figure 2(*a*)) [5]. These kinetic instabilities ($\omega \gg \omega_{ci}$, existing above 100 MHz) are directly observed in these plasmas using high-frequency magnetic pick-up loops in quiescent RE regime [6–8]. Additionally, a lower frequency mode ($\omega \ll \omega_{ci}$) triggered by RE following massive argon injection is found to suppress RE beam formation. Spatiotemporally resolved HXR measurements using the GRI system have also validated RE distribution function $f(E)$ dependencies, demonstrating that decreasing synchrotron damping shifts the high-energy $f(E)$ towards higher energy,
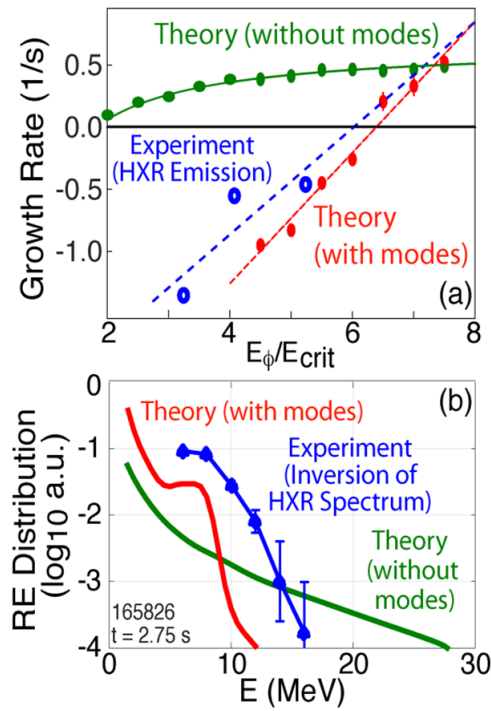
Figure 2. Comparison of measured (blue) and theoretical (red, with kinetic instabilities, and green, without kinetic instabilities) (*a*) RE growth rates and (*b*) RE distribution function.

and increasing collisional damping shifts the full $f(E)$ to lower energy. Agreement between the predicted and measured $f(E)$ is greatly improved when the effect of kinetic instabilities is included (figure 2(*b*)). Observation of these instabilities and their effect on RE dissipation both improves confidence that model-based optimization of RE avoidance and mitigation can be achieved and opens possible new avenues for RE control.

2.2. Transport physics

The inclusion of a reduced physics model for EP transport, known as the *kick model* [9], in TRANSP has resulted in a dramatic improvement in simulating the fast-ion transport during strong Alfvénic activity and tearing modes [10]. Fast-ion transport driven by MHD instabilities can be detrimental to plasma performance on DIII-D and in future burning plasma devices. Figure 3 examines a discharge containing a large 2/1 neoclassical tearing mode (NTM), where the deviation between the measured and (classically) simulated neutron rates indicate substantial fast ion transport. Converting the measured NTM island width into the input mode amplitude for the kick modeling gives a resulting neutron rate that compares well to experiment. Alternatively, if the amplitude of the NTM used in the kick modeling is adjusted to match the measured neutron rate, then good agreement is obtained between predicted and measured NTM island amplitude (figure 3(*a*) inset) and FIDA signal for counter-passing ions (figure 3(*c*)), as well as satisfactory FIDA agreement for co-passing ions (figure 3(*b*)). The phase space resolution implemented in the kick modeling is crucial for reproducing details of the measured beam ion profile from FIDA. Enhancements to TRANSP via
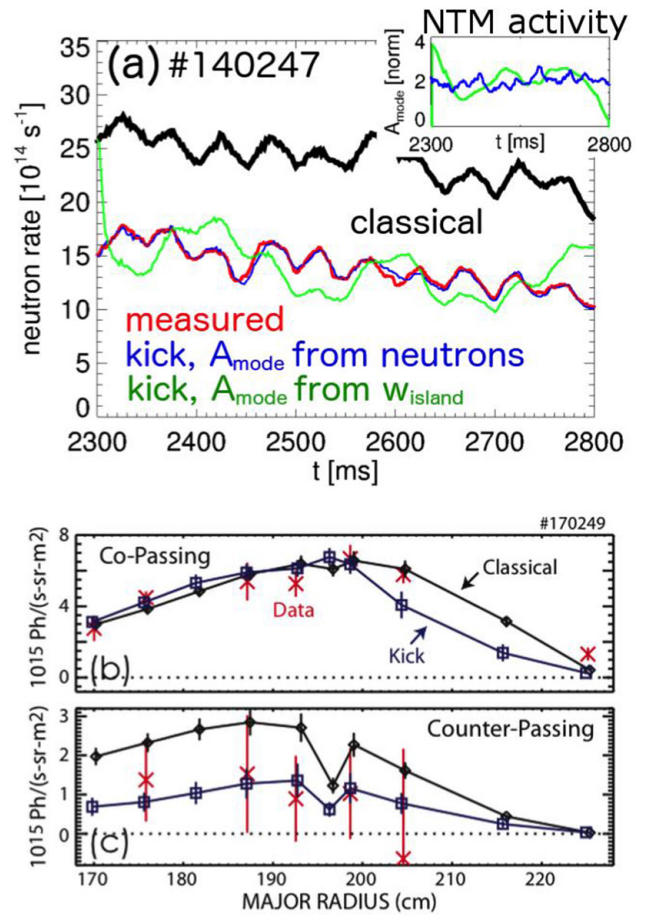

Figure 3. (*a*) Neutron rate from classical prediction (black), kick modeling (blue and green) and experiment (red). The inset shows the mode amplitude from interpretive kick model analysis (blue) and experiment (green). Radial profiles for FIDA signals for (*b*) co- and (*c*) counter-passing fast ions from classical prediction (black), kick modeling (blue) and experiment (red).

the inclusion of reduced EP transport models enable scenario development and predictions including realistic treatment of fast ion transport by instabilities.

The predicted toroidal rotation profile in ITER from intrinsic and NBI sources is significant enough to have a stabilizing influence on turbulent transport, thereby enhancing ITER's fusion performance. The measured ρ^* and ν^* scaling of intrinsic torque with NBI sources predicts an edge rotation in ITER of 10 krad s^{-1} [11], while a dimensionless empirical scaling for intrinsic rotation gives a slightly lower value of 4 krad s^{-1} [12]. Using the lower value, figure 4 shows that the predicted rotation profile for the ITER baseline scenario (IBS) made with the TGYRO and TGLF transport model, and including the NBI torque, has enough $\boldsymbol{E} \times \boldsymbol{B}$ shear to double the D–T fusion gain compared to no shear simulations [13]. While these initial experiments were conducted using NBI heating, subsequent experiments in ECH H-mode plasmas find a similar ρ^* scaling of intrinsic angular momentum, showing that any effect of the fast ions on previous results were unimportant for this ITER rotation prediction. Additionally, differences in intrinsic rotation for closed and open divertor configurations are small, showing that momentum transport
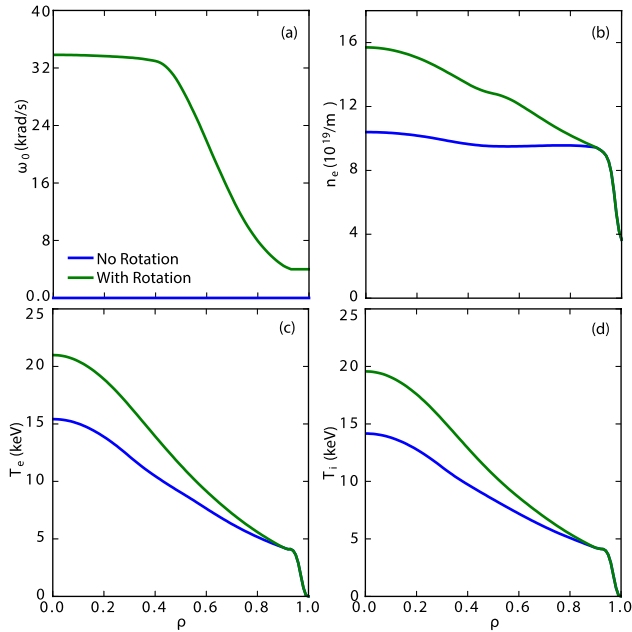
Figure 4. Predictions of ITER baseline scenario from TGYRO and TGLF, with and without $E \times B$ shear effects: (a) toroidal rotation with 4 krad/s boundary condition, (b) electron density, (c) electron temperature and (d) ion temperature.
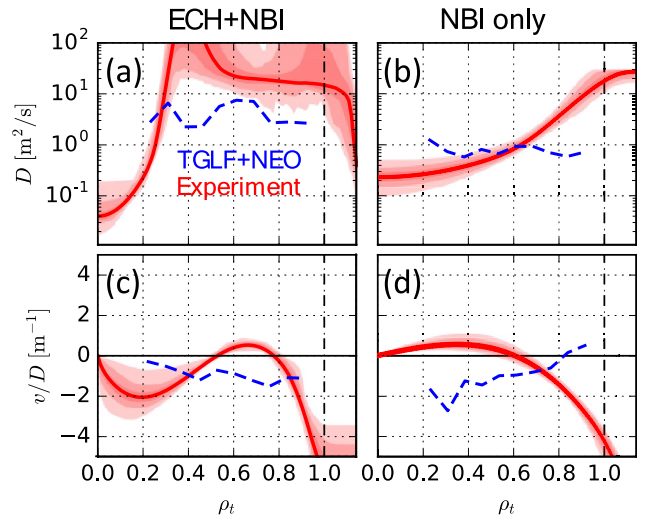

Figure 5. Measured ((a) and (b)) aluminum diffusion and ((c) and (d)) density peaking factor (red lines) for ECH + NBI with $T_e/T_i = 1.6$ and NBI only with $T_e/T_i = 0.7$. Modeled aluminum transport from TGLF and NEO are also indicated (dash blue lines).

due to neutrals in the pedestal is not a significant hidden variable. Besides the effect on turbulence, the toroidal rotation profile in ITER may affect ELM suppression physics, as discussed in section 3.2.

An investigation of metallic impurity transport using the recently installed LBO system in DIII-D [14] demonstrates little core accumulation of aluminum in ITER-relevant H-mode plasmas. Measuring metallic impurity accumulation is beneficial for constraining multi-channel transport models and helps predict fuel dilution in ITER. By varying the mix of electron cyclotron heating (ECH) and NBI, the transport of a trace amount of aluminum has been probed for H-mode plasmas with $T_e/T_i = 0.7$ and 1.6 at fixed density (4×10^{19} m^{-3}) and fixed beam torque (2 Nm) [15]. Propagation of the aluminum is monitored by a combination of fast soft-x ray diagnostic and charge exchange spectroscopy of the fully striped ions. Using the STRAHL model, the transport coefficients that best reproduce the observed emissivity evolution are shown in figure 5 by red confidence bands. A large increase in impurity diffusion at $T_e/T_i = 1.6$ is observed just outside of the ECH location at $\rho = 0.25$, while the density peaking factor v/D is small in both cases. Aluminum transport predictions from the TGLF-SAT0 transport model [16] and NEO neoclassical code [17], indicated by blue dashed lines in figure 5, similarly find a small value of v/D. While the modeled aluminum diffusion for the $T_e/T_i = 1.6$ case is 5–10 times larger than the $T_e/T_i = 0.7$ case, it is below the experiment value during ECH. Future experiments using the LBO system on DIII-D will extend these impurity transport studies in ITER-relevant conditions to higher-Z ions like tungsten.

Studies of negative triangularity (δ) shape find reduced fluctuations and H-mode like confinement ($H_{98y2} = 1.2$) in plasmas with L-mode like edge pressure profiles and no

ELMs, with high beta ($\beta_N = 2.7$) operation achieved. These experiments used a combination of ECH and NBI to explore regimes with $T_e/T_i > 1$ and $T_e/T_i \sim 1$ [18, 19]. Plasmas with $\delta = -0.4$ have the same global performance as a positive triangularity ($\delta = 0.4$) ELMy H-mode discharge with the same plasma current, elongation and area. Interestingly, a power scan up to 10 MW in negative triangularity plasmas shows little evidence of degradation in the energy confinement time, as seen in figure 6, in contrast to the characteristic decrease in τ_E with higher heating power in confinement scaling relations such as ITER-89P [20]. Preliminary fluctuation data shows that negative δ plasmas have lower levels of density and electron temperature fluctuations, typically reduced by 20% in the region $0.7 < \rho < 1.0$, compared to equivalent positive δ discharges. A linear gyrokinetic analysis indicates that improved core confinement in negative δ discharges is from reduced growth rates in the spectral region $k_\theta \rho_s < 2$ due to effect of shape on the dominant TEM modes.

2.3. Divertor detachment physics

In boundary physics, a primary method of reducing the divertor heat flux is to establish highly radiating boundary plasmas with cold, dissipative conditions in front of the divertor targets ('detachment'). As shown in figure 7, UEDGE multi-fluid simulations [21] with cross-field drifts ($B \times \nabla B$-drift towards the X-point) have been able to reproduce the experimentally observed step-like onset of divertor detachment (difference between the black and red symbols and lines) in H-mode plasmas by running simulations with the same boundary conditions but different initial guesses for the divertor neutral density [22, 23]. The bifurcation of the divertor solution between the attached and detached branches is being driven by the non-linear dependence of divertor $E \times B$-drifts on the divertor conditions and potentials. In low density, high temperature attached conditions, the strong radial potential gradient between the common scrape-off layer (SOL) and
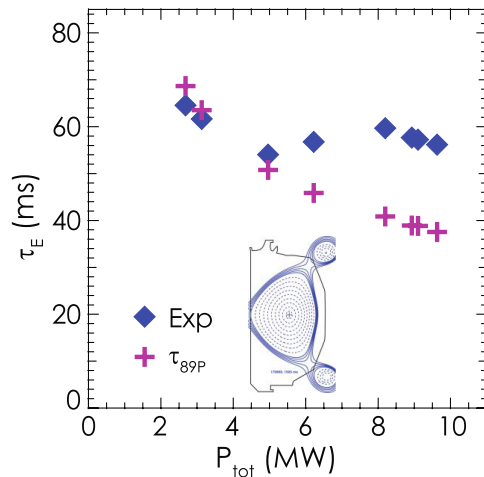
Figure 6. Measured energy confinement time (blue diamonds) versus total heating power for negative triangularity discharges with an L-mode edge. The expected τ_E from the ITER-89P confinement scaling relation (red crosses) is plotted for reference.
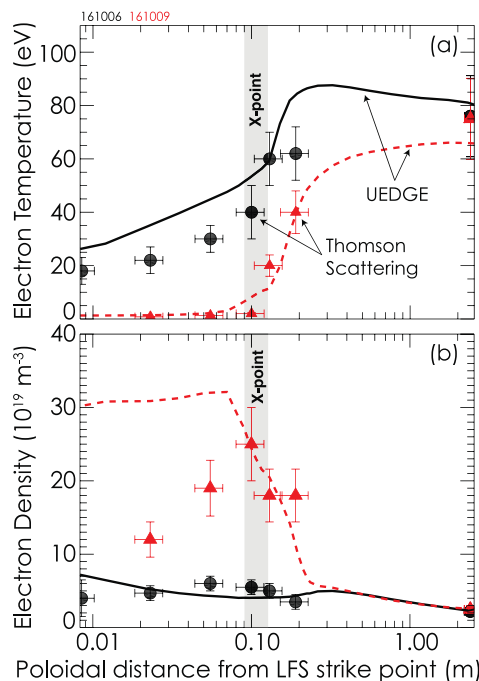

Figure 7. Measured and simulated (*a*) electron temperature and (*b*) electron density along a flux tube in the LFS SOL. Black symbols and line are an attached case, red is a detached case. The UEDGE simulations correspond to $\Psi_N = 1.0009$.

private flux region (PFR) drives a poloidal $\boldsymbol{E} \times \boldsymbol{B}$-drift from the low field side (LFS) to the high field side (HFS) divertor, maintaining low density, high temperature attached conditions. As the divertor evolves towards detachment, the strong radial potential gradient between common SOL and PFR is reduced, diminishing the $\boldsymbol{E} \times \boldsymbol{B}$-drift particle sink in the LFS divertor leg. As a result, the LFS divertor leg can evolve nonlinearly to strongly detached conditions with minimal change in the upstream SOL plasma density.

The excellent divertor diagnostics on DIII-D have been used to characterize the upstream SOL conditions and divertor parallel transport in detached H-mode plasmas [24].
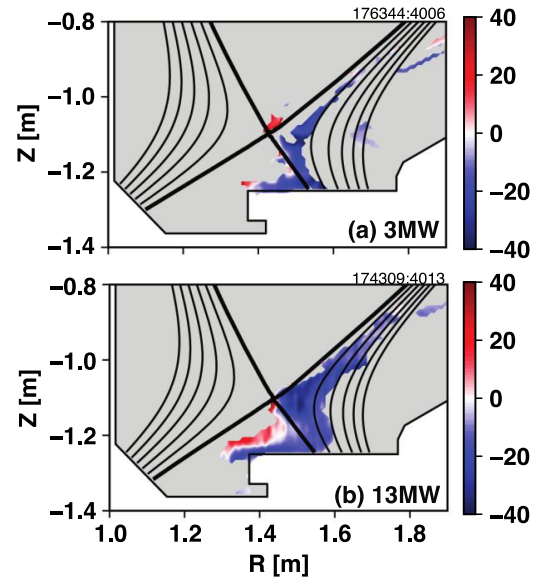

Figure 8. Coherence imaging spectroscopy of toroidal flow of C-III impurity for (*a*) 3 MW case and (*b*) 13 MW case. Negative flow velocity (blue) is towards the divertor target.

Experiments find that the midplane separatrix density for detachment increases approximately as the square root of the parallel heat flux, as expected from analytic 1D models of conduction dominated heat flux. However, the divertor density does not increase with power as expected, indicating that parallel convection (rather than conduction) carries a significant fraction of the power through the radiating zone, expanding the radiating region from the *X*-point towards the divertor target. Imaging of the C-III flow velocity by CIS [25], shown in figure 8, finds a parallel plasma flow towards the divertor target at near the sound speed ($M \sim 1$), which may account for the observed parallel heat flux profile (not shown). In addition, the significantly larger volume of C-III emission in the divertor with higher power seen in figure 8 indicates increased radial transport, leading to a broader density profile.

2.4. Tungsten erosion physics

As ITER will have stringent limits on tungsten (W) core contamination, recent model validation studies have sought to improve the understanding of high-Z gross and net erosion in a mixed-materials divertor environment through benchmarking against DIII-D plasma material interaction (PMI) experiments. ERO modeling of L-mode DiMES experiments and results from the DIII-D experiments with W rings embedded in the lower divertor indicate that high-Z erosion and migration in the DIII-D divertor is strongly influenced by the transport and deposition of low-Z impurities [26, 27]. In the Metal Rings Campaign, two 5 cm wide, toroidally symmetric rings of W-coated tiles were installed in the lower divertor. The W gross erosion rate was measured by a high-resolution CCD-based camera with a filter for W-I 400.9 nm spectral line intensity and the effective ionization/photon (S/XB) coefficients. The global carbon impurity transport with the background plasma condition reconstructed by the Onion Skin Model
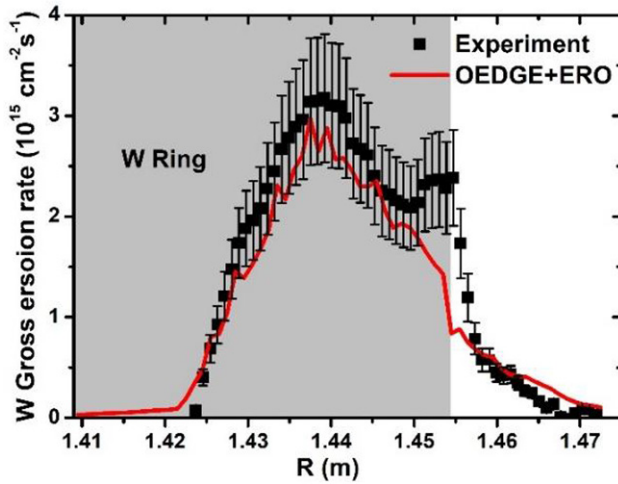
Figure 9. Comparison of experimental and ERO modeled tungsten gross erosion rate as a function of major radius.
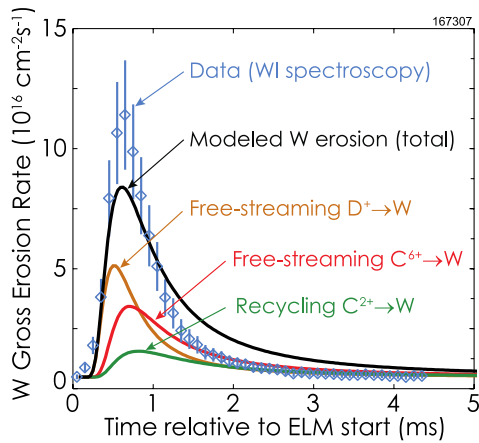

Figure 10. FSRM predictions of the gross erosion rate of tungsten versus ELM time with the contributions from different W erosion pathways identified. Measurements inferred from W–I spectroscopy are overlaid (blue diamonds).

is simulated using the OEDGE code, which can provide the local incident flux and energy of C ions with different charge states for the ERO simulations. With the assumption of additional C from the first wall region, the ERO simulations taking into account the material mixing model can well reproduce the measured W gross erosion rate profile in the radial direction, as shown in figure 9 [28].

A refined model for the ELM heat and particle flux to the divertor, the free-streaming plus recycling model (FSRM) [29, 30], has been tested against DIII-D databases of ELM ion fluence and W gross erosion measurements and found to be consistent across a wide range of pedestal and divertor conditions using a constant value of 0.96 for the effective particle recycling coefficient [31, 32]. The measured gross erosion rate of a W-coated DiMES sample during an ELM cycle is shown in figure 10. The predicted gross erosion rate of W from the FSRM is overlaid, showing reasonable agreement although the experiment exhibits a sharper peak and a faster decay time. Looking at the individual contributions from the FSRM, the energetic free-streaming D^+ ions and C^{6+} impurities from the
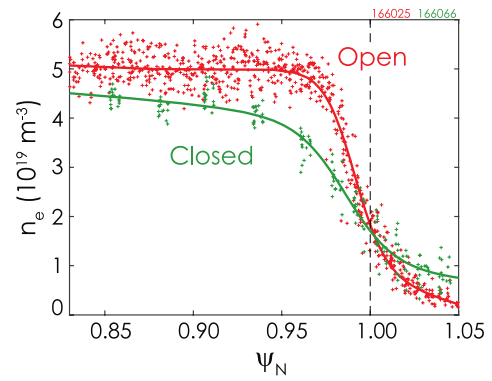

Figure 11. Comparison of H-mode pedestal densities with matched separatrix values for open LSN divertor (red) and closed USN divertor (green) configurations. In both cases the $\boldsymbol{B} \times \boldsymbol{\nabla B}$-drift direction is toward the X-point.

pedestal top dominate the intra-ELM gross erosion of W in the DIII-D divertor. This understanding supports the idea of replacing carbon with lower Z ions (Li, Be) for better erosion control, plasma impurity content, and tritium retention in future fusion reactors.

3. Core-edge integration

Developing fully integrated core-pedestal-SOL-divertor solutions remains a significant challenge for magnetic fusion, spanning plasma physics, atomic physics, and plasma-material interactions. Understanding these linkages to inform solutions is the goal of core-edge integration research.

3.1. Effect of neutrals on pedestal density

Experiments find that divertor geometry, and specifically divertor closure (the ability to confine neutrals), can be used as a tool to change the pedestal structure to allow the probing of pedestal transport over a range of n_e and T_e gradients. On DIII-D, an open divertor configuration can be obtained with discharges in a lower-single-null (LSN) configuration with the outer strike point (OSP) on the lower shelf, while a closed configuration can be obtained with an upper-single-null (USN) configuration with the OSP in the throat of the baffled upper pump. Figure 11 shows that, at the same separatrix density, the H-mode pedestal density is ≈20% lower for the closed divertor configuration [33]. Modeling with both OEDGE and SOLPS shows that for similar T_e and n_e profiles near the OSP, the closed divertor has a significant reduction (up to 50%) in the amount of core ionization as compared to the open divertor [33–35]. Combined with increased SOL dissipation, the lower ratio of $n_{e,ped}/n_{e,sep}$ for the closed divertor results in the onset of divertor detachment occurring at ≈40% lower pedestal density than for the open divertor, making the cold, dissipative divertor more compatible with a hot, low collisionality core. Furthermore, the lower ratio of $n_{e,ped}/n_{e,sep}$ for the closed divertor allows access to pedestals with a larger outward shift of the electron density gradient relative to the electron temperature gradient than is obtained with the open divertor [36].
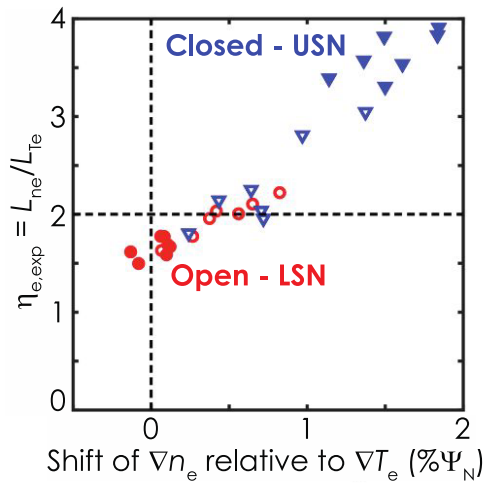
Figure 12. Variation of η_e at maximum pedestal electron pressure gradient in open (red) and closed (blue) divertor geometries versus the difference between locations of maxima of n_e and T_e gradients. Filled symbols are for partially detached divertors.
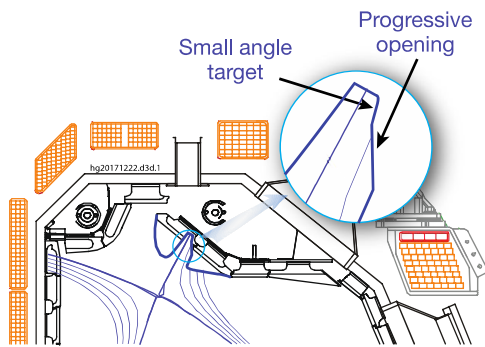

Figure 13. Schematic of prototype small angle slot (SAS) divertor. Inset shows blowup of slot geometry.

As seen in figure 12, the ratio of $\eta_e = L_{ne}/L_{Te}$, with L_{ne} and L_{Te} being the n_e and T_e scale lengths respectively, increases approximately linearly with the gradient shift parameter such that η_e is varied by more than a factor of two. The high values of η_e achieved (~4) show that a large gradient of T_e can be maintained even with flattening of the density pedestal. This is a promising result for ITER, which is predicted to have a flat density pedestal.

A SAS divertor has been installed on DIII-D (figure 13) to further evaluate the role of divertor closure in achieving efficient heat dispersal required for steady-state tokamaks. SAS was designed to both enhance neutral trapping and optimize neutral distribution along the target to achieve strong plasma cooling across the divertor at a lower upstream plasma density [37, 38]. Experiments have found a strong impact of drifts on SAS operation, and showed that with the ion $\boldsymbol{B} \times \boldsymbol{\nabla B}$-drift away from the X-point SAS can achieve, relative to both the open LSN divertor and the more closed USN divertor, (i) a significant reduction of the electron temperature across the divertor target and (ii) access to dissipative divertor operation with $T_e < 10\,\mathrm{eV}$ over a wider range of H-mode operational densities. As seen in figure 14, SAS divertor obtains detachment at lower plasma density for well-matched discharges
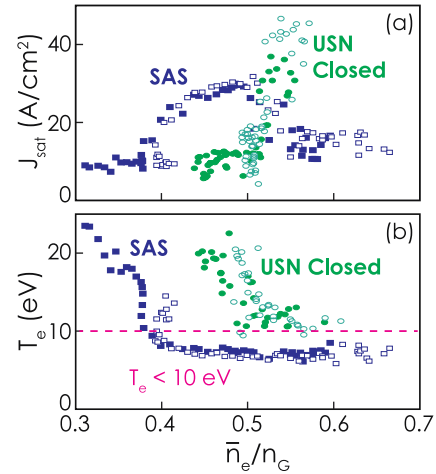

Figure 14. Comparison of (*a*) Langmuir probe ion saturation current density and (*b*) electron temperature near strike point versus line-averaged density normalized to the Greenwald density limit for SAS (blue) and closed upper divertor (green).
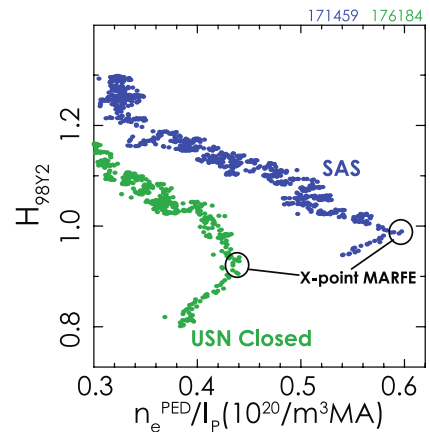

Figure 15. Comparison of IPB98(y, 2) confinement factor versus pedestal density normalized to plasma current for SAS (blue) and closed upper divertor (green). Densities for X-point MARFE formation are also indicated.

without impurity radiation enhancement at $I_P \sim 1\,\mathrm{MA}$ and $P_{NB} \sim 4\,\mathrm{MW}$ [39].

The SAS discharges exhibit less degradation in H-mode confinement factor with increasing edge pedestal density than the closed USN divertor for similar conditions, as plotted in figure 15. Detailed transport and pedestal stability analyses find that the better confinement with SAS is associated with improved pedestal temperature and pressure, which are primarily due to an increased pedestal width. Also shown in figure 15 are the densities where an X-point MARFE results in further confinement reduction (circled points). For the SAS discharges, there is a greater range of density between detachment onset and X-point MARFE formation, thus widening the window for detachment control and facilitating core-edge integration.

Experiments studying neutral particle fueling indicate that a lower particle source inside the separatrix from higher opacity SOL is not necessarily a barrier to raising the pedestal density [40]. Relating the midplane filterscope signals

to the neutral density gives evidence that the ionization front is pushed further out into the SOL during strong gas puffing, increasing the opaqueness to neutrals. An up-down asymmetry in the electron density on closed surfaces (i.e. higher densities closer to X-point) is measured for the first time in ELMy H-mode on DIII-D at higher fueling rates. While the measured change in the edge density during gas puff modulation shows that direct neutral fueling is inefficient for opaque SOL conditions, the outer divertor leg appears to detach with increasing opacity/SOL density, which can explain the continued increase in pedestal density if the ionized plasma in the SOL flows to the divertor and there recycles, proving a new pathway to fuel the core plasma.

3.2. Effect of RMP on plasma edge

DIII-D has made major advances in using 3D magnetic fields to extend ELM suppression and pedestal performance. Reduced ELM suppression thresholds and dynamic divertor control have been obtained using a rotating $n = 2$ RMP combined with a stationary $n = 3$ RMP [41, 42]. Experiments have demonstrated that using mixed toroidal harmonic RMP for ELM suppression lowers the threshold coil current by ~10% (a 30% decrease in the equivalent current of total energy) compared to a RMP with a single toroidal harmonic number. In these experiments, $n = 2$ RMP is only able to mitigate ELMs, while complete ELM suppression is achieved with $n = 3$ RMP. For the ELM mitigation case, a linear dependence of the plasma response on the applied field is measured, but when the two RMPs are combined a jump up in $n = 3$ plasma response is observed during the transition from ELM mitigation to suppression. This jump is a non-linear bifurcation that indicates the $n = 2$ field helps to penetrate the $n = 3$ mode which leads to ELM suppression. MHD simulation with the MARS-F code [43] shows good agreement in both mode structure and phase from magnetic sensors during ELM mitigation, although during ELM suppression the modeling has an unexplained phase shift relative to the observed plasma response in DIII-D. Prominent heat flux splitting in the divertor is observed in these experiments for $n = 3$ RMP, as seen in figure 16, while variation of the heat flux splitting pattern is observed when $n = 2$ RMP is added at different phases [44]. The particle flux footprint on the divertor shows a similar behavior as the heat flux. These patterns are qualitatively consistent with modeling of field penetration depth using TOP2D [45] with plasma response modeled by MARS-F. Therefore, the fine structure in the divertor heat and particle flux during ELM suppression can be smoothed out during a full cycle of a rotating $n = 2$ RMP (combined with a static $n = 3$ RMP). These results expand the physics understanding and potential effectiveness of this multi-harmonic technique for reliably controlling ELMs and divertor power/particle loading distributions in future burning plasma devices as ITER.

Previous work on DIII-D demonstrated that ELM suppression with $n = 3$ RMP in the IBS is lost when the injected NBI torque is reduced below ~4 Nm [46]. Experiments on DIII-D have since focused on resolving the cause of this apparent
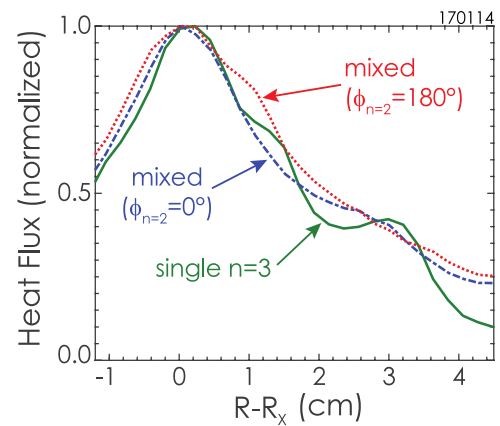

Figure 16. Measured divertor heat flux profiles for pure $n = 3$ RMP (green), and additional $n = 2$ RMP with phase 0° (blue) and 180° (red).

rotation threshold by conducting NBI torque scans using co- and counter-I_P sources in the ITER similar shape (ISS) with $q_{95} = 3.5$ [47]. Figure 17(a) shows that a clear and consistent edge carbon impurity rotation threshold (V_ϕ) for maintaining RMP ELM suppression of about 10 km s^{-1} is found (Mach no. $M_\phi \sim 0.1$) regardless of core plasma pressure. Within the field penetration paradigm for ELM suppression [48], this can be explained by an inward motion of the zero-crossing of the flow, which moves the region of field penetration too far away from the pedestal top if rotation is too low [49]. Indeed, computing the $\boldsymbol{E} \times \boldsymbol{B}$ rotation profile (ω_E) for the final ELM suppressed time-slice reveals a critical location for the ω_E zero-crossing of $\Psi_N = 0.91$ (figure 17(b)). Narrowing the pedestal by reducing the upper triangularity is found to move the critical ω_E zero-crossing radius outward, suggesting a critical distance between the pedestal top and the ω_E zero-crossing. These studies also are unable to find any critical condition for the electron perpendicular rotation, challenging two-fluid models of field penetration.

While no simple beam torque threshold describes the ELMy/suppressed boundary in figure 17, a negative value for the edge beam torque *density* is a good predictor of losing RMP ELM-suppression [47]. It is important to note that balanced NBI with 'zero injected torque' is modeled by NUBEAM [50] to yield a edge localized torque in the counter-I_P direction owing to the loss of trapped counter beam ions after the first bounce (i.e. counter beam orbit loss torque). Therefore, rather than discuss ITER-relevant torques, a semi-quantitative requirement on ITER's edge rotation for RMP ELM-suppression is derived from the scaling of the toroidal flow required to sustain an ω_E zero-crossing. Along a dimensionally similar path, the Mach no. at $E_r = 0$ scales like $M_\phi \sim q\rho^*$ (i.e. diamagnetic scaling) [13]. Thus, the $M_\phi \sim 0.1$ threshold for the ISS on DIII-D scales to $M_\phi \sim 0.02$ on ITER, which is an edge rotation of ~3 km s^{-1} or ~0.4 krad s^{-1}. This threshold estimate is well below the predicted edge rotation from intrinsic torque on ITER shown in figure 4(a) (albeit without RMP), indicating a favorable scaling for obtaining ELM-suppression in ITER.
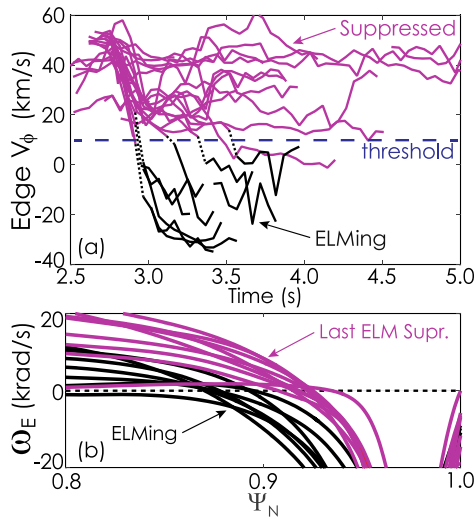
Figure 17. Low-torque ISS with applied $n = 3$ RMP showing ELMy and ELM-suppresses cases: (*a*) edge rotation of carbon impurity, and (*b*) $\boldsymbol{E} \times \boldsymbol{B}$ rotation profile versus normalized poloidal flux.

Figure 18. $\boldsymbol{E} \times \boldsymbol{B}$ velocity profile before L–H transition, as measured by DBS, with and without applied RMP. The expected edge magnetic stochastic layer is shaded. Dash line shows predicted $\boldsymbol{E} \times \boldsymbol{B}$ velocity from a simple fluid model of stochasticity for the largest $\delta B/B$ case.

Figure 19. Density fluctuation spectra before L–H transition, measured by BES, with and without applied RMP.

Studies on DIII-D find that the increase in H-mode threshold power from $n = 3$ RMP becomes larger for ITER-relevant collisionalities, which is potentially a concern for ITER since RMP may have to be applied prior to the L–H transition to safely suppress the first ELM. Experiments in the ISS with a mix of ECH and balanced NBI, $\langle n_e \rangle = 1.5\text{–}5 \times 10^{19}$ m^{-3} and $q_{95} \sim 3.6$ demonstrate that the L-H power threshold with applied RMP increases with decreasing collisionality like $P_{LH} \sim \nu^{*-0.3}$, compared to non-RMP plasmas where $P_{LH} \sim \nu^{*-0.1}$ [51]. The L-H power threshold is impacted above a threshold $\delta B/B \sim 2.5 \times 10^{-4}$, which is below the ELM suppression threshold. Similar to earlier RMP investigations in L-mode plasmas [52], a reduction in the $\boldsymbol{E} \times \boldsymbol{B}$ velocity well and $\boldsymbol{E} \times \boldsymbol{B}$ shear, extracted from poloidal turbulence advection measured by Doppler backscattering (DBS), is observed just before the L–H transition (see figure 18). For the highest $\delta B/B$ case, reversal of the $\boldsymbol{E} \times \boldsymbol{B}$ drift is observed. These changes in the edge radial electric field (E_r) are accompanied by an increase in long wavelength turbulence measured by beam emission spectroscopy (BES), as plotted in figure 19. Edge magnetic stochasticity provides an attractive explanation of the edge plasma modifications and increase in P_{LH} with RMP, and the more pronounced decrease in edge E_r well at low ν^* is consistent with a simple fluid model describing stochastic electron current flow (dash line in figure 18). Preliminary experiments indicating that $n = 3$ non-resonant magnetic perturbations give rise to smaller changes in E_r and $\boldsymbol{E} \times \boldsymbol{B}$ shear suggest there is room for optimization of the RMP spectrum with less effect on P_{LH}.

Impurity experiments using $n = 3$ RMP fields to suppress ELMs in ITER-shaped plasmas found a factor of 2–3 reduction in the effective helium particle confinement time compared to ELMy H-modes without RMP fields [53]. Measurements of neutral partial pressures in the pumping plenum from Penning gauges show the partial pressure of helium incr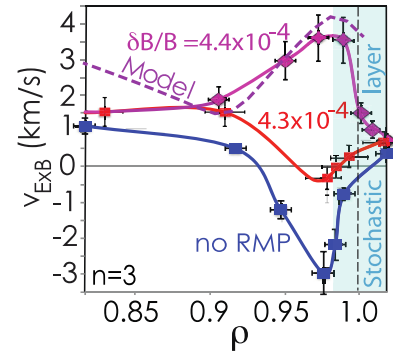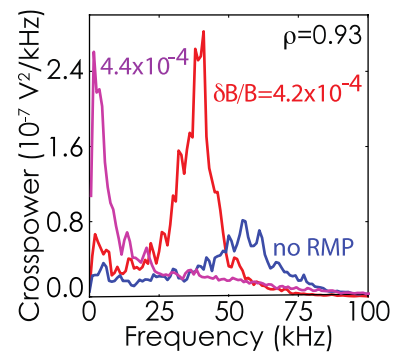eases substantially more than that of deuterium during RMP ELM-suppression for a range of cases, in comparison with ELMy cases. This result suggests that RMP fields may generate adequate helium ash removal in ITER in the absence of ELM events.

Finally, the Super H-mode regime, which achieves high confinement and high beta with an elevated pedestal height and broad profiles [54, 55], has been utilized to create high fusion performance plasmas with reduced divertor heat flux. Super H-mode is predicted by the EPED model [56] to occur in strongly shaped plasmas where the pedestal solution remains peeling limited (pressure increasing with density) up to very high density. By extending the Super H-mode regime to high I_P (up to 2 MA), very high pedestal pressures (~30 kPa) and record stored energies (3.2 MJ) for the present DIII-D vessel configuration have been transiently achieved [57], as shown in figure 20, with $\beta_{N,ped} = 1.3$ and $H_{98y2} = 1.6\text{–}2.4$. During the density rise phase shortly after the L–H transition, the Super H-mode attains peak values of D–T equivalent fusion gain that are the highest achieved (=0.45) on any medium scale ($R < 2$ m) tokamak. By applying a small $n = 3$ RMP to the Super H-mode regime to control the density and impurity accumulation, good performance has been sustained for ~3 s at $\beta_N = 2.9$, $H_{98y2} = 1.6$ and nearly 2 MJ of stored energy. Because the pedestal in Super H-mode is limited by current-driven modes, it is predicted that the near separatrix density can be increased to enable attractive divertor solutions while remaining compatible with high fusion performance in the
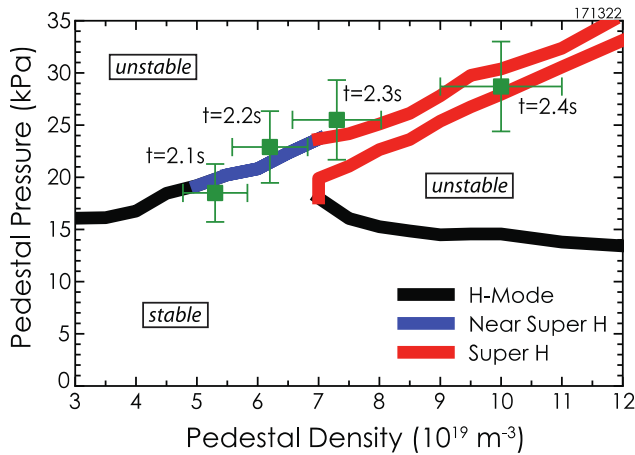
Figure 20. EPED prediction of pedestal pressure as a function of density based on high triangularity ($\delta = 0.56$), $I_P = 1.6$ MA discharge. Green symbols are measured values.
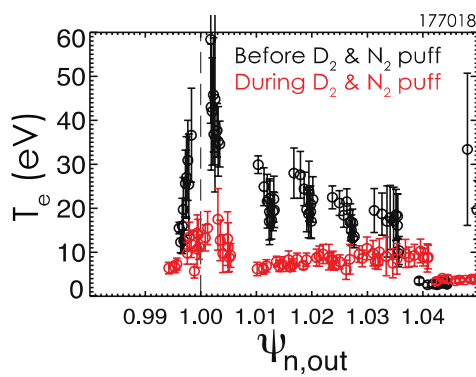

Figure 21. Measurement of outer divertor electron temperature in Super H-mode before (black) and during (red) a combination of D_2 and N_2 fueling.

core. New experiments have employed D_2 and N_2 gas puffing to improve divertor conditions. High pedestal pressure (>20 kPa) and $H_{98y2} \approx 1.1$ are sustained in a strongly radiating divertor with a high gas puff rate and more than a factor-of-2 reduction in divertor electron temperature (see figure 21).

4. Scenario development

Research into scenario development aims to unite all of the elements needed for a specific burning plasma mission. In this area, recent DIII-D activity has emphasized the coupling of stable, low-rotation inductive scenarios to methods of ELM suppression, as well as joining a high power, high beta core to a radiative divertor solution.

4.1. Low-torque inductive scenarios for ITER

A key result from IBS experiments in DIII-D is that stable (although dense) plasmas with zero injected torque can achieve normalized plasma pressures capable of generating 500 MW of fusion power in ITER, as well as a fusion gain metric insensitive to plasma current between $2.8 \leqslant q_{95} \leqslant 3.7$ [58, 59]. Previous attempts at IBS with zero beam torque
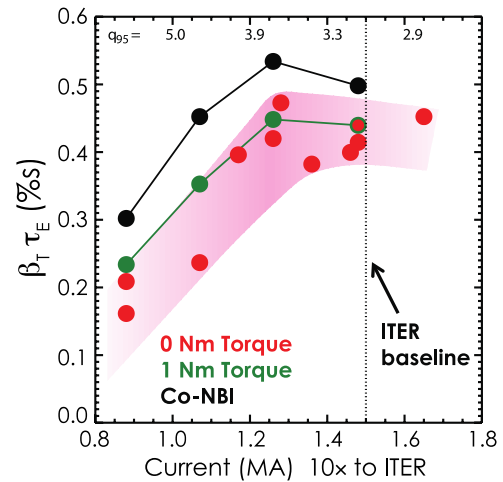

Figure 22. Fusion gain metric ($\beta\tau_E$) as a function of plasma current (lower abscissa) and safety factor (upper abscissa) for different levels of injected beam torque.

were impeded by a disruptive $n = 1$ tearing mode; analysis of a DIII-D database of previous stable and unstable IBS plasmas concluded that the $n = 1$ tearing mode stability is correlated with the depth of the 'well' in the current density just inside the bootstrap-driven peak in the edge current density [60]. This result motivated new experiments to modify the current density profile at the beginning of the stationary pressure phase by slowing the current ramp rate, delaying the L–H transition time, and raising the density prior to the L–H transition. Additionally, the ELM frequency is regularized by a low-level gas flow to give a more consistent pedestal condition. A DIII-D shape well matched to the ITER separatrix is used such that a normalized current (I_P/aB_T) of 1.4 yields $q_{95} \approx 3$. Plasma current scans are performed with three levels of injected beam torque: full co-NBI, 1 Nm and zero torque. Feedback control of the neutral beams maintains simultaneously the normalized pressure and injected torque using duty cycle modulation of the co- and counter-sources. Stable operation with zero injected torque is obtained down to $q_{95} = 2.8$, while a volume average beta of 2.55%, able to produce 500 MW of fusion power in ITER, is achieved at a higher value of $q_{95} \approx 3.4$. For co-NBI a volume average beta of 2.55% is reached for $q_{95} \approx 4.2$. The fusion gain metric ($\beta\tau_E$) shows saturation with decreasing q_{95} for all levels of applied torque (see figure 22). The same $\beta\tau_E$ is obtained for $q_{95} = 3.7$ as for $q_{95} = 2.8$ with zero injected torque, but the lower current case has lower disruption risk. Further work in IBS development in DIII-D is needed to extend the zero injected torque plasmas to lower density to better match ITER's collisionality.

Experiments in DIII-D have advanced the quiescent H-mode (QH-mode) regime toward becoming a natural solution to avoid ELMs in a zero injected torque, high confinement scenario that is compatible with strong electron heating and ITER's collisionality. Investigations of the newly developed wide-pedestal QH-mode, which exhibits a transport-limited pedestal regulated by broadband turbulence when the NBI torque is ramped from strongly counter-I_P towards zero [61–63], have revealed that this regime can operate over a
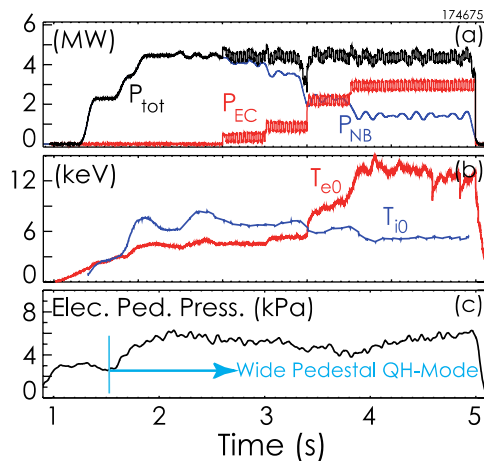
Figure 23. Wide pedestal QH-mode discharge replacing NBI with ECH at constant total power: (*a*) NBI, ECH and total heating powers, (*b*) central electron and ion temperatures, and (*c*) electron pedestal pressure.

large range of NBI torques fully covering the scaled ITER-equivalent NBI torque. Recently the strong counter-I_P start-up torque has been eliminated so that the entire discharge uses essentially zero (0.04 to -0.06 Nm) NBI torque [64]. The ~ 0 injected torque operation greatly benefits from using NTV from $n = 3$ RMP fields to maintain enough plasma rotation to prevent core tearing modes from growing and locking [65]. Turning off the NTV torque after formation of the wide-pedestal has little effect on the discharge. Scans of the NBI power in wide-pedestal QH-mode have found no degradation in energy confinement time, resulting in a H_{98y2} confinement factor that increases with heating power up to 1.6. Furthermore, the wide-pedestal QH-mode regime has been sustained for several confinement times with dominant electron heating (ratio of ECH to NBI power of 4:1) and low torque (-0.9 Nm). Depositing the ECH power at $\rho = 0.2$ results in an electron internal transport barrier (ITB) with T_e exceeding 12 keV, as shown in figure 23. More generally, the observed improvement in both core and pedestal confinement as T_e/T_i approaches 1 and the continued ELM-stable operation with high power ECH suggests that fast ions from NBI (including the associated counter beam orbit loss torque) are not a requirement for wide-pedestal QH-mode. Also the operating space for wide-pedestal QH-mode has been expanded to include a lower-single-null configuration with the ITER triangularity value and a range of safety factors ($4.3 < q_{95} < 7.5$, transiently 3.8). For this range of q_{95}, the maximum volume average beta obtained without ELMs is $\beta = 2.1\%$ ($\beta_N = 2.3$). Thus, QH-mode looks to be a promising ELM-stable scenario for ITER if fusion performance targets ($\beta = 2.55\%$, $q_{95} \approx 3$) can be reached—a key remaining challenge.

4.2. Steady-state scenarios for ITER

The high-β_P scenario with high q_{min} ($\geqslant 3$) has been extended inductively from $q_{95} \sim 11$ to $q_{95} \sim 6$ while maintaining an ITB and H_{98y2} above 1.5 [66]. One of the key characteristics of this scenario is the large radius ITB in all transport channels,
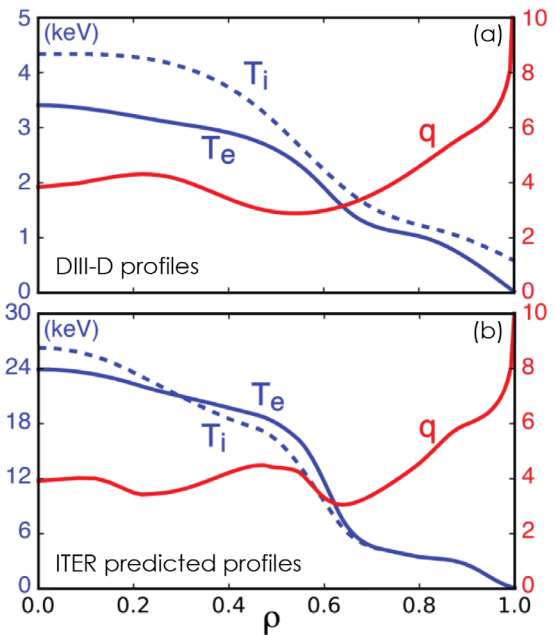

Figure 24. Electron temperature, ion temperature and safety factor for high β_P scenario with $q_{95} \sim 6$: (*a*) measured profiles from DIII-D discharge with strong ITB, and (*b*) TGYRO prediction for ITER steady-state scenario with zero $E \times B$ shear.

which is due to the Shafranov shift stabilization of turbulence at large β_P [67]. These experiments utilize a second I_P ramp up during the high beta phase ($\beta_N \sim 2.6$–3.0) to increase the plasma current from 0.6 MA to 1.0 MA. The ITB can be maintained even as β_P is reduced due to a strong reverse magnetic shear near $\rho \sim 0.5$, as seen in figure 24(*a*), confirming predictions that negative central shear can lower the β_P threshold for the ITB. Experiments at q_{95} relevant for steady-state reactors have found two observed confinement states for the same β_P: (i) a H-mode confinement state with a high edge pedestal, and (ii) an enhanced confinement state at lower NBI power with a low edge pedestal and an ITB. The ITB formation can be explained through Shafranov shift stabilization creating a bifurcation in transport. The transition between these two confinement states may be related to changes in the pedestal region. When applying a large $n = 3$ RMP to the high-β_P scenario to mitigate large type-I ELMs, no transition is found to the enhanced confinement state which is otherwise observed with smaller $n = 3$ perturbations. This is consistent with the hypothesis that a large edge perturbation may be needed to trigger the bifurcation to an ITB state. Pedestal stability analysis using ELITE shows that the high pedestal, H-mode state is limited by the current gradient, whereas the ITB state with low pedestal is far away from both the peeling and ballooning limits. Self-consistent modeling of this high-β_P regime using the TGYRO code to predict the density, temperature and safety factor profiles, as shown in figure 24(*b*), finds that the reverse magnetic shear and ITB can be maintained on ITER using the day-one current drive systems, leading to a $Q = 5$ steady-state scenario without needing strong $E \times B$ shear.

Finally, a substantial expansion of the high-β_N hybrid scenario to high density and radiating divertor operation has been achieved, and shows how the electron heating location impacts
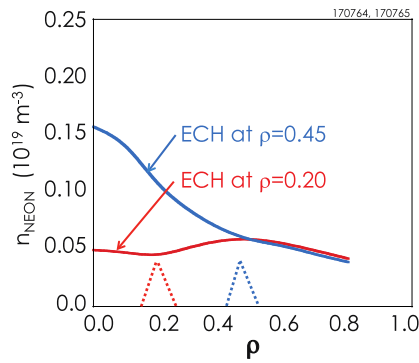
Figure 25. Comparison of neon impurity densities for high-β_N hybrid scenario with near-axis and off-axis ECH deposition and trace neon flow (~0.6 Torr l s^{-1}).

Figure 26. Lower divertor heat flux, measuring by an IR camera, for high-β_N hybrid scenario with and without (*a*) neon injection (3.60 Torr l s^{-1}) and (*b*) argon injection (1.54 Torr l s^{-1}).

the effectiveness of a radiating mantle solution. Coupling a high-performance core to a divertor with acceptable heat flux is a crucial step for any fusion reactor. Previously DIII-D developed a low-collisionality steady-state hybrid scenario with $q_{95} = 5.5$–6.5 that reaches ~85% of the ideal MHD 'with wall' β_N limit and scales to $Q = 5$ on ITER [68–71]. To integrate this scenario with divertor heat flux mitigation using the 'puff-and-pump' technique entails increasing the pedestal density by ~50% or more, which requires moving ECH from $\rho \sim 0.05$–0.2 to $\rho = 0.45$ to avoid the density cutoff [72]. These experiments find that higher density improves confinement and pedestal height at high heating power ($P_{tot} > 12$ MW), partially due to improved pedestal stability from decoupling of the peeling and ballooning branches [73]. While these plasmas run reliably with $\beta_N \leqslant 3.8$, $H_{98y2} = 1.6$ and 56 MJ of injected energy from ECH and NBI, the change in ECH location has a strong effect on the profiles of the neon and argon ions used to create a radiating mantle. For off-axis ECH, the density profile peaking factor is ~2.6 for neon and ~3.2 for argon, both of which are more peaked than the electron density profile (~1.4); for on-axis ECH, the neon profile is flat and no accumulation is observed (see figure 25). Radiating emissivity measurements show an increased radiative peaking in the edge region (as desired for a radiating mantle) compared to cases without impurities; however, an increase in core radiation due to central impurity accumulation with off-axis ECH is correlated with significant fuel dilution and an onset of 5/2 and/or 3/1 tearing modes. Owing to the impurity/MHD complications with off-axis ECH, so far a modest 40% reduction in between-ELM divertor heat flux has been achieved with argon-based and neon-based mantles, as displayed in figure 26 [74]. A low injected torque is also a necessary condition for reactor-relevant studies, and this has been assessed in the high-β_N hybrid regime using a mixture of co- and counter-NBI. Scanning the NBI torque from 8.5 Nm (full co-injection) to 0.5 Nm (best match of co- and counter-NBI power), up to the available 4.5 MW of counter-NBI power, finds that the H_{98y2} factor systematically decreases from 1.55 to 1.07. For the lowest torque condition, the H_{98y2} factor is independent of ECH power. Future experiments will combine low injected torque and radiative divertor operation by utilizing increased ECH power with a higher density limit (either from higher
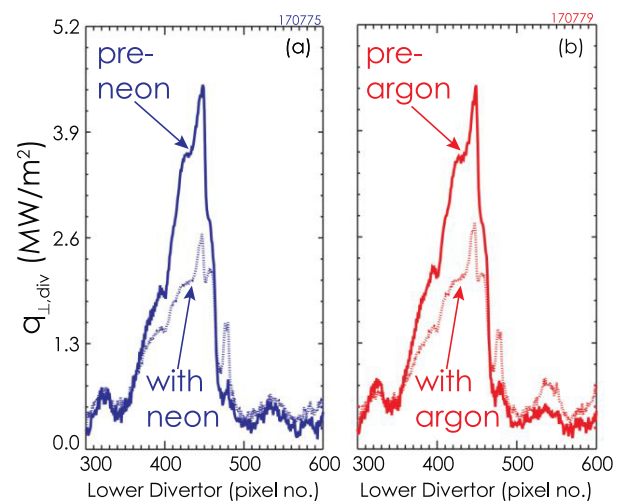
frequency gyrotrons or 2nd harmonic O-mode absorption) and central deposition, along with improved divertor closure to help localize impurity pumping, to prevent central impurity accumulation.

5. Summary and future plans

The DIII-D program is addressing critical challenges for ITER and the next generation of fusion devices through research on plasma physics fundamentals, integration of disparate core and boundary plasma physics, and development of attractive scenarios. Disruption mitigation experiments injecting multiple shattered pellets find that simultaneously injected pellets may impact the assimilation of each other and alter the resulting disruption characteristics. Better resolved measurements and more comprehensive modeling of RE dissipation on DIII-D have provided a resolution to widely observed anomalous RE dissipation results [75], improving confidence that RE mitigation and avoidance can be predictively optimized. The inclusion of a *kick model* for EP transport in TRANSP has resulted in a dramatic improvement in simulating fast-ion transport during strong Alfvénic activity and tearing modes. Measurements of the ρ^* dependence of intrinsic rotation in ECH H-modes find similar ρ^* scaling as for NBI H-modes, and the predicted $E \times B$ rotational shear for ITER is large enough to give significant turbulence stabilization. In boundary physics, UEDGE multi-fluid simulations show that the $E \times B$-drifts can explain the sharp onset of detachment since a positive feedback mechanism helps the density to rise more rapidly and accelerate detachment. Detached divertor plasmas display characteristics of convection dominated transport with parallel plasma flows towards the divertor target of $M \sim 1$. Recent model validation studies conclude that energetic free-streaming D$^+$ ions and C^{6+} impurities from the pedestal top typically dominate the intra-ELM gross erosion of W in the DIII-D divertor.

In core-edge integration, a closed divertor configuration is found to reduce core ionization and access flatter pedestal density profiles, while allowing a large gradient of pedestal T_e can be maintained. Experiments with the new SAS divertor achieved a significant reduction in T_e across the divertor target and access to dissipative divertor operation at lower density with respect to the other two (open/closed) divertor configurations on DIII-D. At high SOL opacity, gas puffing does not appear to play a direct role in raising the pedestal density since the particle source inside the separatrix is actually reduced; the ionized plasma in the SOL may flow to the outer detached divertor leg and recycle. Using a rotating $n = 2$ RMP combined with a stationary $n = 3$ RMP, the equivalent coil current for ELM suppression is reduced by ~30% and the fine structure in the divertor heat and particle fluxes are smoothed out. For RMP ELM suppression in the ITER similar shape ($q_{95} = 3.5$), a clear and consistent threshold in the impurity rotation of ~10 km s^{-1} is observed at which point ELM suppression is lost, possibly due to the inward motion of the ω_E zero-crossing; fortunately, this scales to a threshold value in ITER that is less than the expected pedestal rotation from intrinsic torque. The increase in P_{LH} with RMP is higher for ITER relevant collisionalities and is likely explained by a reduction in the edge E_r well and $E \times B$ shear from edge magnetic stochasticity. In the Super H-mode regime, very high pedestal pressure (>20 kPa) and core confinement are sustained with a strongly radiating divertor and a $>2 \times$ reduction in divertor electron temperature.

A key advance in scenario development has been the achievement of stable (although dense) ITER baseline discharges with zero injected torque and a fusion gain metric insensitive to plasma current between $2.8 \leqslant q_{95} \leqslant 3.7$. In the wide pedestal QH-mode regime that exhibits improved performance, operation with ≈ 0 injected NBI torque over the entire discharge and compatibility with dominant electron heating have been demonstrated. The high-β_P scenario with high q_{min} ($\geqslant 3$) has been extended inductively from $q_{95} \sim 11$ to $q_{95} \sim 6$ while maintaining an ITB with the help of strong reverse magnetic shear near $\rho \sim 0.5$. The high-β_N hybrid scenario has been extended to high density and radiating divertor operation with $\beta_N \leqslant 3.8$ and $H_{98y2} = 1.6$; both argon-based and neon-based radiating mantles achieve a 40% reduction in divertor heat flux but a large difference in core impurity peaking is observed between central and off-axis ECH deposition. These scenario experiments have made substantial progress in integrating all of the necessary ingredients for a burning plasma device: low torque, ELM suppression, electron heating, confinement enhancement, high density, radiating divertors and impurity transport.

After 2018, DIII-D research will orient further to the steady-state path [76], doubling its off-axis NBI power by vertically tilting two beam sources as well as making them toroidally steerable for co- or counter-injection, and doubling the electron cyclotron power to raise T_e/T_i at low torque, increase off-axis current drive and allow perturbative transport studies under high performance conditions. DIII-D will also explore new methods of high efficiency off-axis current drive to optimize the high-beta, steady-state path, including

top-launch ECCD and 1 MW helicon wave current drive at 476 MHz in 2019, and inside-launch LHCD soon after. We are currently optimizing the alignment of the upper SAS tiles with the toroidal field and associated diagnostic upgrades. This is accompanied by plans for new high-Z tiles in the upper SAS divertor to enable study of high-Z leakage from closed divertors, and in the future more reactor-relevant pumped slot divertors. Disruption mitigation research will test silicon shell pellets filled with silicon or boron. Additional power supplies and a new 3D coil set are planned to explore the physics basis for optimization of ELM and MHD control. Critical physics questions will be addressed with new diagnostics including multi-channel divertor Thomson scattering to inform detachment studies, divertor charge exchange spectroscopy for T_i measurements, expanded 3D-magnetic diagnostics, EUV imaging to look at the earliest stages of runaway electron formation, a fast ion loss detector optimized for reverse B_T direction (preferred for off-axis NBI), a wall interaction tile station for rapid evaluation of first wall materials and PMI, imaging MSE, and expansions and upgrades to the existing suite of turbulence diagnostics.

Acknowledgments

Disclaimer

This report was prepared as an account of work sponsored by an agency of the United States Government. Neither the United States Government nor any agency thereof, nor any of their employees, makes any warranty, express or implied, or assumes any legal liability or responsibility for the accuracy, completeness, or usefulness of any information, apparatus, product, or process disclosed, or represents that its use would not infringe privately owned rights. Reference herein to any specific commercial product, process, or service by trade name, trademark, manufacturer, or otherwise does not necessarily constitute or imply its endorsement, recommendation, or favoring by the United States Government or any agency thereof. The views and opinions of authors expressed herein do not necessarily state or reflect those of the United States Government or any agency thereof.

Appendix. The DIII-D team

L. Abadie[1], T.W. Abrams[2], J. Ahn[3], T. Akiyama[4], P. Aleynikov[5], J. Allcock[6], E.O. Allen[2], S. Allen[7], J.P. Anderson[2], A. Ashourvan[8], M.E. Austin[9], J. Bak[10], K.K. Barada[11], N. Barbour[8], L. Bardoczi[12], J. Barr[2], J.L. Barton[13], E.M. Bass[14], D. Battaglia[8], L.R. Baylor[3], J. Beckers[15], E.A. Belli[2],

J.W. Berkery[16], N. Bertelli[8], J.M. Bialek[16], J.A. Boedo[14], R.L. Boivin[2], P.T. Bonoli[17], A. Bortolon[8], M.D. Boyer[8], R.E. Brambila[2], B. Bray[2], D.P. Brennan[8], A.R. Briesemeister[3], S.A. Bringuier[2], M.W. Brookman[2], D.L. Brower[11], B.R. Brown[2], W.D. Brown[8], D. Buchenauer[13], M.G. Burke[18], K.H. Burrell[2], J. Butt[8], R.J. Buttery[2], I. Bykov[14], J.M. Candy[2], J.M. Canik[3], N.M. Cao[17], L. Carbajal Gomez[3], L.C. Carlson[2], T.N. Carlstrom[2], T.A. Carter[11], W. Cary[2], L. Casali[12], M. Cengher[2], V.S. Chan[19], B. Chen[19], J. Chen[20], J. Chen[11], M. Chen[21], R. Chen[20], Xi Chen[2], W. Choi[16], C. Chrobak[2], C. Chrystal[2], R.M. Churchill[8], M. Cianciosa[3], C.F. Clauser[14], M. Clement[16], J. Coburn[22], C.S. Collins[2], A.W. Cooper[23], B.M. Covele[2], J.W. Crippen[2], N.A. Crocker[11], B.J. Crowley[2], A. Dal Molin[24], E.M. Davis[17], J.S. deGrassie[2], C.A. del-Castillo-Negrete[25], L.F. Delgado-Aparicio[8], A. Diallo[8], S.J. Diem[3], R. Ding[12], S. Ding[12], W. Ding[11], J.L. Doane[2], D.C. Donovan[26], J. Drake[2], D. Du[2], H. Du[27], X. Du[28], V. Duarte[8], J.D. Duran[26], N.W. Eidietis[2], D. Elder[29], D. Eldon[2], W. Elwasif[3], T.E. Ely[2], K.M. Eng[2], K. Engelhorn[2], D. Ennis[30], K. Erickson[8], D.R. Ernst[17], T.E. Evans[2], M.E. Fenstermacher[7], N.M. Ferraro[8], J.R. Ferron[2], D.F. Finkenthal[31], P.A. Fisher[8], B. Fishler[2], S.M. Flanagan[2], J.A. Fooks[2], L. Frassinetti[32], H.G. Frerichs[18], Y. Fu[33], T. Fulop[34], Q. Gao[27], F. Garcia[2], A.M. Garofalo[2], A. Gattuso[2], L. Giacomelli[35], E.M. Giraldez[2], C. Giroud[36], F. Glass[2], P. Gohil[2], X. Gong[20], Y.A. Gorelov[2], R.S. Granetz[17], D.L. Green[37], C.M. Greenfield[2], B.A. Grierson[8], R.J. Groebner[2], W.H. Grosnickle[2], M. Groth[38], H.J. Grunloh[2], H.Y. Guo[2], W. Guo[20], J. Guterl[12], R.C. Hager[8], S. Hahn[10], F.D. Halpern[2], H. Han[39], M.J. Hansink[2], J.M. Hanson[16], J. Harris[2], S.R. Haskey[8], D.R. Hatch[9], W.W. Heidbrink[28], J. Herfindal[3], D.N. Hill[2], M.D. Hill[40], E.T. Hinson[18], C.T. Holcomb[7], C.G. Holland[14], L.D. Holland[2], E.M. Hollmann[14], A.M. Holm[38], R. Hong[12], M. Hoppe[34], S. Houshmandyar[9], J. Howard[41], N.T. Howard[17], Q. Hu[8], W. Hu[20], H. Huang[2], J. Huang[20], Y. Huang[20], G.A. Hughes[2], J. Hughes[17], D.A. Humphreys[2], A.W. Hyatt[2], K. Ida[4], V. Igochine[5], Y. In[42], S. Inoue[43], A. Isayama[43], R.C. Isler[3], V.A. Izzo[14], M.R. Jackson[2], A.E. Jarvinen[7], Y. Jeon[10], H. Ji[33], X. Jian[19], R. Jimenez[2], C.A. Johnson[30], I. Joseph[7], D.N. Kaczala[2], D.H. Kaplan[2], J. Kates-Harbeck[44], A.G. Kellman[2], D.H. Kellman[2], C.E. Kessel[8], K. Khumthong[2], C.C. Kim[45], H. Kim[10], J. Kim[46], K. Kim[12], S.H. Kim[1], W. Kimura[47], J.R. King[48], A. Kirk[36], K. Kleijwegt[15], M. Knolker[8], A. Kohn[5], E. Kolemen[8], M. Kostuk[2], G.J. Kramer[8], P. Kress[49], D.M. Kriete[18], R.J. La Haye[2], F.M. Laggner[33], H. Lan[20], M.J. Lanctot[2], R. Lantsov[11], L.L. Lao[2], C.J. Lasnier[7], C. Lau[12], K. Law[3], D. Lawrence[50], J. Le[51], R.L. Lee[2], M. Lehnen[1], R. Leon[2], A.W. Leonard[2], M. Lesher[2], J.A. Leuer[52], G. Li[20], K. Li[20], K.T. Liao[9], Z. Lin[28], C. Liu[2], C. Liu[8], F. Liu[53], Y. Liu[2], Z. Liu[20], S. Loch[30], N.C. Logan[8], J.M. Lohr[2], J. Lore[3], T.C. Luce[1], N.C. Luhmann[21], R. Lunsford[8], C. Luo[21], Z. Luo[20], L. Lupin-Jimenez[8], A. Lvovskiy[12], B.C. Lyons[2], X. Ma[12], R. Maingi[8], M.A. Makowski[7], P. Mantica[54], M. Manuel[2], M.W. Margo[2], A. Marinoni[17], E. Marmar[17], W.C. Martin[2], R.L. Masline[14], G.K. Matsunaga[43], D.M. Mauzey[8], P.S. Mauzey[2], J.T. Mcclenaghan[12], G.R. Mckee[18], A.G. Mclean[7], H.S. Mclean[7], E. Meier[55], S.J. Meitner[3], J.E. Menard[8], O. Meneghini[2], G. Merlo[11], W.H. Meyer[7], D.C. Miller[2], W.J. Miller[2], C.P. Moeller[2], K.J. Montes[17], M.A. Morales[2], S. Mordijck[49], A. Moser[2], R.A. Moyer[14], S.A. Muller[2], S. Munaretto[2], M. Murakami[3], C.J. Murphy[2], C.M. Muscatello[2], C.E. Myers[13], A. Nagy[8], G.A. Navratil[16], R.M. Nazikian[8], A.L. Neff[37], T.F. Neiser[11], A. Nelson[33], P. Nguyen[2], R. Nguyen[2], J.H. Nichols[26], M. Nocente[24], R.E. Nygren[13], R.C. O'Neill[2], T. Odstrcil[17], S. Ohdachi[4], M. Okabayashi[8], E. Olofsson[2], M. Ono[43], D.M. Orlov[14], T.H. Osborne[2], N.A. Pablant[8], D.C. Pace[2], R.R. Paguio[2], A. Pajares Martinez[56], C. Pan[20], A. Pankin[48], J.M. Park[3], J. Park[8], Y. Park[16], C.T. Parker[2], S.E. Parker[57], P.B. Parks[2], C.J. Pawley[2], C.A. Paz-Soldan[2], W.A. Peebles[11], B.G. Penaflor[2], T.W. Petrie[2], C.C. Petty[2], Y. Peysson[58], A.Y. Pigarov[14], D.A. Piglowski[2], R.I. Pinsker[2], P. Piovesan[59], N. Piper[40], R.A. Pitts[1], J.D. Pizzo[60], M.L. Podesta[8], F.M. Poli[8], D. Ponce[2], M. Porkolab[17], G.D. Porter[61], R. Prater[2], J. Qian[20], O. Ra[42], T. Rafiq[56], R. Raman[55], C. Rand[2], G.C. Randall[2], J.M. Rauch[2], C. Rea[17], M.L. Reinke[3], J. Ren[26], Q. Ren[20], Y. Ren[8], T.L. Rhodes[11], J. Rice[17], T.D. Rognlien[7], J.C. Rost[17], W.L. Rowan[9], D.L. Rudakov[14], A. Salmi[62], B.S. Sammuli[2], C.M. Samuell[7], A.M. Sandorfi[63], C. Sang[64], O.J. Sauter[65], D.P. Schissel[2], L. Schmitz[11], O. Schmitz[18], E.J. Schuster[56], J.T. Scoville[2], A. Seltzman[17], I. Sfiligoi[2], M. Shafer[3], H. Shen[2], T. Shi[20], D. Shiraki[3], H. Si[20], D.R. Smith[18], S.P. Smith[2], J.A. Snipes[1], P.B. Snyder[2], E.R. Solano[66], W.M. Solomon[2], A.C. Sontag[3], V.A. Soukhanovskii[7], D.A. Spong[3], W.M. Stacey[40], G.M. Staebler[2], L. Stagner[12], B. Stahl[2], P.C. Stangeby[29], T.J. Stoltzfus-Dueck[8], D.P. Stotler[8], E.J. Strait[2], D. Su[2], L.E. Sugiyama[17], A.A. Sulyman[21], Y. Sun[20], C. Sung[67], W.A. Suttrop[5], Y. Suzuki[4], A. Svyatkovskiy[33], R.M. Sweeney[1], S. Taimourzadeh[28], M. Takechi[43], T. Tala[62], H. Tan[20], S. Tang[11], X. Tang[68], D. Taussig[2], G. Taylor[8], N.Z. Taylor[12], T.S. Taylor[2], A. Teklu[69], D.M. Thomas[2], M.B. Thomas[70], K.E. Thome[12], A.R. Thorman[41], R.A. Tinguely[17], B.J. Tobias[68], J.F. Tooker[2], H. Torreblanca[2], A. Torrezan De Sousa[2], G.L. Trevisan[12], D. Truong[18], F. Turco[16], A.D. Turnbull[2], E.A. Unterberg[3], P. Vaezi[14], P.J. Vail[33], M.A. Van Zeeland[2], M. Velasco Enriquez[71], M.C. Venkatesh[2], B.S. Victor[7], F. Volpe[16], M.R. Wade[2], M.L. Walker[2], J.R. Wall[2], G.M. Wallace[17], R.E. Waltz[2], G. Wang[11], H. Wang[20], H. Wang[12], Y. Wang[21], Y. Wang[20], Z. Wang[68], Z. Wang[8], F. Wang[64], S.H. Ward[70], J.G. Watkins[13], M. Watkins[2], W.P. Wehner[56], M. Weiland[5], D.B. Weisberg[2], A.S. Welander[2], A.E. White[17], R.B. White[8], D. Whyte[17], T.A. Wijkamp[15], R. Wilcox[3], T. Wilks[17], H.R. Wilson[70], A. Wingen[3], E. Wolfe[8], M. Wu[20], W. Wu[2], S.J. Wukitch[17], T. Xia[20], N. Xiang[20], B. Xiao[20], R. Xie[9], G. Xu[19], H. Xu[2], X. Xu[7], Z. Yan[18], Q. Yang[20], X. Yang[64], M. Yoshida[43], G. Yu[21], J.H. Yu[14], M. Yu[10], S.A. Zamperini[26], L. Zeng[11], B. Zhao[9], D. Zhao[12], H. Zhao[9], Y. Zhao[72], Y. Zhu[21], Y. Zhu[28] and B. Zywicki[73]

Affiliations

[1]ITER Organization
[2]General Atomics
[3]Oak Ridge National Laboratory
[4]National Institute for Fusion Science, Japan
[5]Max-Planck Institute for Plasma Physics
[6]Durham University
[7]Lawrence Livermore National Laboratory
[8]Princeton Plasma Physics Laboratory
[9]University of Texas, Austin

[10]National Fusion Research Institute, Korea
[11]University of California, Los Angeles
[12]Oak Ridge Associated Universities
[13]Sandia National Laboratory
[14]University of California, San Diego
[15]Eindhoven Unversity of Technology
[16]Columbia University
[17]Massachusetts Institute of Technology
[18]University of Wisconsin
[19]University of Science and Technology of China
[20]Institute of Plasma Physics, Chinese Academy of Sciences
[21]University of California, Davis
[22]North Carolina State
[23]EPFL (Lausanne, Switzerland)
[24]Universita di Milano-Bicocca
[25]Stony Brook University (SUNY)
[26]University of Tennessee, Knoxville
[27]Southwestern Institute of Physics, China
[28]University of California, Irvine
[29]University of Toronto
[30]Auburn University
[31]Palomar College
[32]Kungliga Tekniska Hogskolan
[33]Princeton University
[34]Chambers University of Technology (Sweden)
[35]Istituto di Fisica del Plasma CNR-EURATOM
[36]United Kingdom Atomic Energy Authority (CCFE)
[37]Oak Ridge Institute for Science Education
[38]Aalto University
[39]Korea National Fusion Research Center
[40]Georgia Tech
[41]Australian National University
[42]Ulsan National Institute of Science and Technology
[43]National Institutes for Quantum and Radiological Science, Japan
[44]Harvard University
[45]SLS2 Consulting
[46]Far-Tech, Inc.
[47]STI Optronics, Inc.
[48]Tech-X Corporation
[49]The College of William and Mary
[50]General Atomics Temp
[51]Qinzhou University
[52]General Atomics (Retired)
[53]University of Nice
[54]IFP—Consiglio Nazionale delle Ricerche
[55]University of Washington
[56]Lehigh University
[57]University of Colorado, Boulder
[58]CEA Cadarache
[59]Consorzio RFX
[60]Rensselaer Polytechnic Institute
[61]AKIMA Infrastructure Services, LLC
[62]VTT Technical Research Centre
[63]Jefferson Lab
[64]Dalian University of Technology, China
[65]SPC-EPFL
[66]Ciemat
[67]Lam Research Corporation
[68]Los Alamos National Laboratory
[69]Oregon State University
[70]University of York
[71]Universidad Nacional de Ingenieria
[72]Soochow University
[73]University of Michigan

ORCID iDs

C.C. Petty ● https://orcid.org/0000-0003-4534-9073

References

[1] Aymar R. 2002 *Plasma Phys. Control. Fusion* **44** 519
[2] Herfindal J.L. *et al* 2018 Injection of multiple shattered pellets for disruption mitigation in DIII-D *Preprint: 2018 IAEA Fusion Energy Conf. (Gandhinagar, India, 22–27 October 2018)* EX/P6-23
[3] Paz-Soldan C. *et al* 2017 *Phys. Rev. Lett.* **118** 255002
[4] Paz-Soldan C. *et al* 2018 Advances in runaway electron control and model validation for ITER *Preprint: 2018 IAEA Fusion Energy Conf. (Gandhinagar, India, 22–27 October 2018)* EX/6-1
[5] Liu C. *et al* 2018 *Phys. Rev. Lett.* **120** 265001
[6] Spong D.A. *et al* 2018 *Phys. Rev. Lett.* **120** 155002
[7] Thome K.E. *et al* 2018 High-frequency energetic particle driven instabilities and their implications for burning plasmas *Preprint: 2018 IAEA Fusion Energy Conf. (Gandhinagar, India, 22–27 October 2018)* EX/P6-29
[8] Spong D.A. *et al* 2018 Interactions of runaway electrons with Alfvén and Whistler waves *Preprint: 2018 IAEA Fusion Energy Conf. (Gandhinagar, India, 22–27 October 2018)* TH/P8-17
[9] Podesta M. *et al* 2017 *Plasma Phys. Control. Fusion* **59** 095008
[10] Podesta M. *et al* 2018 Reduced energetic particle transport models enable comprehensive time-dependent tokamak simulations *Preprint: 2018 IAEA Fusion Energy Conf. (Gandhinagar, India, 22–27 October 2018)* EX/1-2
[11] Chrystal C. *et al* 2017 *Phys. Plasmas* **24** 056113
[12] DeGrassie J.S. *et al* 2016 *Phys. Plasmas* **23** 082501
[13] Chrystal C. *et al* 2018 Predicting the toroidal rotation profile for ITER *Preprint: 2018 IAEA Fusion Energy Conf. (Gandhinagar, India, 22–27 October 2018)* EX/5-2
[14] Howard N.T. *et al Rev. Sci. Instrum.* submitted
[15] Odstrcil T. *et al* 2018 Turbulent impurity transport in DIII-D plasmas with on-axis electron heating *45th EPS Conf. on Plasma Physics (Prague, Czech Republic, 2018)* (http://ocs.ciemat.es/EPS2018PAP/pdf/P4.1095.pdf)
[16] Staebler G.M. and Kinsey J.E. 2010 *Phys. Plasmas* **17** 122309
[17] Belli E.A. and Candy J. 2008 *Plasma Phys. Control. Fusion* **50** 095010
[18] Austin M.E. *et al* 2018 High confinement in negative triangularity discharges in DIII-D *Preprint: 2018 IAEA Fusion Energy Conf. (Gandhinagar, India, 22–27 October 2018)* EX/P6-6
[19] Austin M.E. *et al Phys. Rev. Lett.* submitted
[20] Yushmanov P.N. *et al* 1990 *Nucl. Fusion* **30** 1999
[21] Rognlien T.D. *et al* 1999 *Phys. Plasmas* **6** 1851
[22] Jaervinen A.E. *et al* 2018 *Phys. Rev. Lett.* **121** 075001
[23] Jaervinen A.E. *et al* 2018 Progress in DIII-D towards validating divertor power exhaust predictions *Preprint: 2018 IAEA Fusion Energy Conf. (Gandhinagar, India, 22–27 October 2018)* EX/9-3

[24] Leonard A.W. *et al* 2018 Parallel energy transport in detached DIII-D divertor plasmas *Preprint: 2018 IAEA Fusion Energy Conf. (Gandhinagar, India, 22–27 October 2018)* EX/P6-12

[25] Samuell C. *et al* 2018 *Phys. Plasmas* **25** 056110

[26] Ding R. *et al* 2016 *Nucl. Fusion* **56** 016021

[27] Wampler W.R. *et al* 2017 *Phys. Scr.* **T170** 014041

[28] Ding R. *et al* 2018 Model validation on EAST and DIII-D experiments towards understanding of high-z material erosion and migration in a mixed materials environment *Preprint: 2018 IAEA Fusion Energy Conf. (Gandhinagar, India, 22–27 October 2018)* MTP/2-2

[29] Fundamenski W. *et al* 2006 *Plasma Phys. Control. Fusion* **48** 109

[30] Moulton D. *et al* 2013 *Plasma Phys. Control. Fusion* **55** 085003

[31] Abrams T. *et al* 2018 *Nucl. Mater. Energy* **17** 164–73

[32] Abrams T. *et al* 2018 Recent advances in understanding tungsten gross erosion during ELMs in the DIII-D divertor *Preprint: 2018 IAEA Fusion Energy Conf. (Gandhinagar, India, 22–27 October 2018)* EX/P6-13

[33] Moser A.L. *et al Phys. Plasmas* submitted

[34] Casali L. *et al* 2018 *Contrib. Plasma Phys.* **58** 725

[35] Sontag A.C. *et al* 2017 *Nucl. Fusion* **57** 076025

[36] Wang H.Q. *et al* 2018 *Nucl. Fusion* **58** 096014

[37] Guo H.Y. *et al* 2017 *Nucl. Fusion* **57** 044001

[38] Shafer M.W. *et al Nucl. Mater. Energy* submitted

[39] Guo H.Y. *et al* 2018 Development and first experimental tests of a small angle slot divertor on DIII-D *Preprint: 2018 IAEA Fusion Energy Conf. (Gandhinagar, India, 22–27 October 2018)* EX/P6-10

[40] Mordijck S. *et al* 2018 Particle transport from the bottom up *Preprint: 2018 IAEA Fusion Energy Conf. (Gandhinagar, India, 22–27 October 2018)* EX/P6-5

[41] Gu S. *et al* 2019 *Nucl. Fusion* **59** 026012

[42] Sun Y. *et al* 2018 Dynamic ELM and divertor control using mixed toroidal harmonic resonant magnetic perturbations in DIII-D and EAST *Preprint: 2018 IAEA Fusion Energy Conf. (Gandhinagar, India, 22–27 October 2018)* EX/7-2

[43] Liu Y.Q. *et al* 2011 *Nucl. Fusion* **51** 083002

[44] Jia M. *et al* 2018 *Phys. Plasmas* **25** 056102

[45] Jia M. *et al* 2016 *Plasma Phys. Control. Fusion* **58** 055010

[46] Moyer R.A. *et al* 2017 *Phys. Plasmas* **24** 102501

[47] Paz-Soldan C. *et al Nucl. Fusion* **59** 056012

[48] Nazikian R. *et al* 2015 *Phys. Rev. Lett.* **114** 105002

[49] Lyons B.C. *et al* 2017 *Plasma Phys. Control. Fusion* **59** 044001

[50] Pankin A. *et al* 2004 *Comput. Phys. Commun.* **159** 157

[51] Schmitz L. *et al* 2018 L–H transition trigger physics in ITER-similar plasmas with and without applied $n = 3$ magnetic perturbations *Preprint: 2018 IAEA Fusion Energy Conf. (Gandhinagar, India, 22–27 October 2018)* EX/4-2

[52] Mordijck S. *et al* 2016 *Plasma Phys. Control. Fusion* **58** 014003

[53] Hinson E.T. *et al* 2018 Enhancement of helium exhaust during suppression of edge localized modes by resonant magnetc perturbation fields at DIII-D *Preprint: 2018 IAEA Fusion Energy Conf. (Gandhinagar, India, 22–27 October 2018)* EX/P6-18

[54] Solomon W. *et al* 2014 *Phys. Rev. Lett.* **113** 135001

[55] Snyder P.B. *et al* 2015 *Nucl. Fusion* **55** 083026

[56] Snyder P.B. *et al* 2011 *Nucl. Fusion* **51** 103016

[57] Snyder P.B. *et al* 2018 High fusion performance in super H-Mode experiments on Alcator C-Mod and DIII-D *Preprint: 2018 IAEA Fusion Energy Conf. (Gandhinagar, India, 22–27 October 2018)* EX/2-4

[58] Luce T.C. *et al Nucl. Fusion* to be submitted

[59] Luce T.C. *et al* 2018 Exploring an alternative approach to $Q = 10$ in ITER *Preprint: 2018 IAEA Fusion Energy Conf. (Gandhinagar, India, 22–27 October 2018)* PPC/2-1

[60] Turco F. *et al* 2018 *Nucl. Fusion* **58** 106053

[61] Burrell K.H. *et al* 2016 *Phys. Plasmas* **23** 056103

[62] Chen X. *et al* 2017 *Nucl. Fusion* **57** 022007

[63] Chen X. *et al* 2017 *Nucl. Fusion* **57** 086008

[64] Ernst D.R. *et al* 2018 Viability of wide pedestal QH-mode for burning plasma operation *Preprint: 2018 IAEA Fusion Energy Conf. (Gandhinagar, India, 22–27 October 2018)* EX/2-2

[65] Garofalo A.M. *et al* 2011 *Nucl. Fusion* **51** 083018

[66] McClenaghan J. *et al* 2018 Transport barriers in DIII-D high β_P plasmas and development of candidate steady state scenarios for ITER *Preprint: 2018 IAEA Fusion Energy Conf. (Gandhinagar, India, 22–27 October 2018)* EX/4-3

[67] Garofalo A.M. *et al* 2017 *Phys. Plasmas* **24** 056114

[68] Turco F. *et al* 2015 *Phys. Plasmas* **22** 056113

[69] Petty C.C. *et al* 2016 *Nucl. Fusion* **56** 016016

[70] Petty C.C. *et al* 2017 *Nucl. Fusion* **57** 116057

[71] Nazikian R. *et al* 2018 *Nucl. Fusion* **58** 106010

[72] Turco F. *et al* 2018 Integration of the high-β_N hybrid scenario to a high performance pedestal, stable zero torque operation, and a divertor solution *Preprint: 2018 IAEA Fusion Energy Conf. (Gandhinagar, India, 22–27 October 2018)* EX/3-3

[73] Petrie T.W. *et al* 2017 *Nucl. Fusion* **57** 086004

[74] Petrie T.W. *et al* 2018 High performance double-null plasmas under radiating divertor and mantle scenarios on DIII-D *Preprint: 2018 IAEA Fusion Energy Conf. (Gandhinagar, India, 22–27 October 2018)* EX/P6-11

[75] Granetz R. *et al* 2014 *Phys. Plasmas* **21** 072506

[76] Buttery R.J. *et al* 2018 *J. Fusion Energy* **38** 72